FINAL TECHNICAL REPORT: Award Number G11AP20047 The Mechanics of Episodic Tremor and Slip: Implications for Seismic Hazards in Cascadia

March 7, 2013

Paul Segall
(650-723-7241, segall@stanford.edu)
Geophysics Department
Stanford University
Stanford, CA 94305-2215

Award Dates: 1/2011 – 12/31/2012

Abstract We continue development of physical models of slow slip events based on dilatant strengthening. Rate-state frictional weakening allows transient slip to nucleate. As the shear rate increases, pores dilate, and restricted pore fluid flow makes the fault zone increasingly undrained. This decreases pore pressure and so increases the frictional resistance to further slip. The faster the fault slips, the harder it is for fluid flow into the fault zone to keep up with dilatancy; thus the stabilizing effect increases with slip speed. However, if slip becomes fast enough, frictional heat is generated leading to thermal pressurization, and fast slip.

Slow slip events (SSE) in many subduction zones incrementally stress the adjacent locked megathrust, suggesting that they could potentially either trigger or evolve into damaging earthquakes. We explore this with 2D quasi-dynamic simulations with rate-state friction, dilatancy, and coupled 1D pore-fluid and heat transport. Steady-state weakening friction allows transient slip to nucleate, but is inhibited by dilatant strengthening and destabilized by thermal pressurization. SSE spontaneously nucleate in Low Effective-Stress Velocity-Weakening (LESVW) regions. If the dimension of the LESVW is relatively small the SSE are trapped at its updip end, imparting a strong stress concentration in the locked zone. After several centuries SSE penetrate into the region of higher effective stress, where thermal pressurization eventually leads to dynamic rupture. For larger LESVW regions SSE tend to increase in length with time; ultimately higher slip speeds enhance thermal weakening, leading to dynamic instability within the SSE zone. In both cases the onset of the ultimate SSE is essentially indistinguishable from preceding events.

The predictions of the physics-based model are compared with GPS observations, both during and between SSE events. The fit to average SSE displacements using the inferred distributions of frictional properties and effective normal stress is remarkably good, suggesting that the the low effective stress – velocity weakening region is in roughly the correct depth

range. The fit to the inter-ETS data is not as good, but seems to imply modest interseismic creep (≤ 12 mm/yr) at depths of $\lesssim 20$ km.

The numerical methods have been improved to include the effects of flash heating, finite thickness shear zones, and to 3D (2D faults). Work on accelerating the 3D calculations continues. We have also developed Hierarchical-matrix (H-matrix) compression software library `hmmvp`, that allows computation of Boundary Element calculations in $O(n \log n)$ time, rather than $O(n^2)$ time for uncompressed matrix vector products.

1 Report

In this report we present results to a number of questions raised in the proposal.

How does the model behavior depend on depth-dependent frictional properties and effective stress, including the effects of finite thickness shear zones? Segall and Bradley [2012a] present two-dimensional quasi-dynamic simulations that include rate-state friction, dilatancy, and heat and pore fluid flow normal to the fault. We find that at lower background effective normal stress ($\bar{\sigma}$), slow slip events occur spontaneously, whereas at higher $\bar{\sigma}$, slip is dynamic. At intermediate $\bar{\sigma}$, dynamic events are followed by quiescent periods, and then long periods of repeating slow slip events. In these cases, accelerating slow events ultimately lead to dynamic rupture. Zero-width shear zone approximations [Segall et al., 2010] are adequate for slow slip events, but substantially overestimate the pore pressure and temperature changes during fast slip.

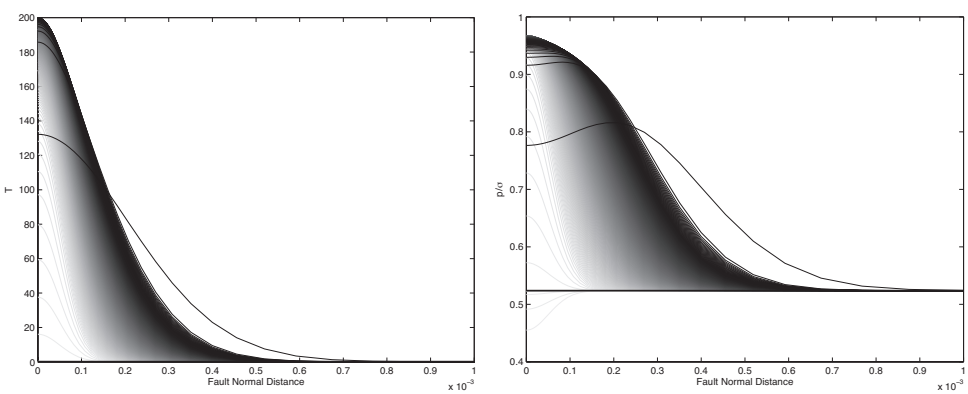

Figure 1: a) Temperature (°C) and b) pore pressure (p/σ) vs fault normal distance during dynamic slip with uniform properties. $h = 100\mu$m, $d_c = 10\mu$m; the effective d_c for dilatancy was scaled by $h/h_c = 1/10$. $\sigma - p^\infty = 100$ MPa, $W/L_c = 30$.

The governing equations are given in Segall and Bradley [2012a]. We extended the constitutive law for dilatancy and compaction [Segall and Rice, 1995], motivated by experiments [Marone et al., 1990, Samuelson et al., 2009], to account for a finite thickness shear zone, h. We assume that the change in porosity integrated across the shear zone per unit slip is independent of h. This predicts that the net porosity change, proportional to the change in shear zone thickness, scales linearly with h, consistent with some lab data [Marone and Kilgore, 1993]; as does the length scale over which dilatancy approaches steady state.

For normal stresses of order 100 MPa, the zero-width approximation leads to extreme shear heating during seismic slip. This is ameliorated by including a finite thickness fault. For the simulation in Figure 1 the effective d_c for dilatancy (only) was scaled by $h/h_c = 1/10$, such that the effective d_c for dilatancy is small and the consequent increase in effective stress occurs with

very little slip. Even so, the temperature rise was limited to 200°C, compared to > 1000°C in the zero-width case. The pore pressure is limited to $\sim 0.95\sigma$, compared to $p/\sigma > 1$ in the zero-width case.

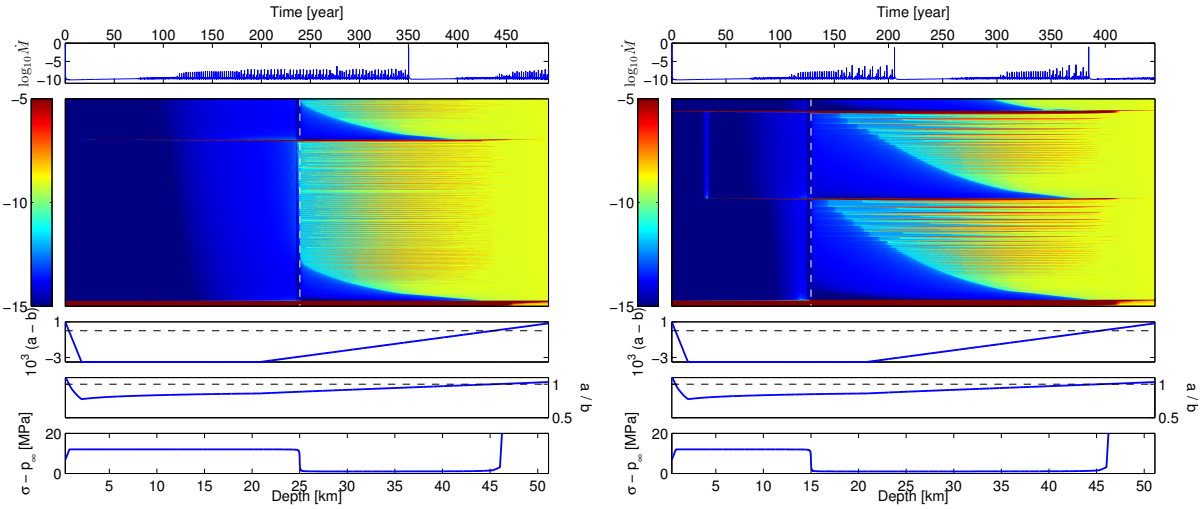

Figure 2: Two modes of SSE triggering dynamic slip events. Top panel shows spatially averaged slip speed with time, showing dynamic events and regularly spaced SSE. Next panel shows space-time distribution of slip rate (logarithmic color scale) with depth scale on bottom. Time (vertical axis, from bottom to top) is proportional to solver time steps. Bottom plots show depth distribution $a - b$, a/b, and $\bar{\sigma}$, as a function of depth. (a) Low $\bar{\sigma}$ region extending from 25 to 45 km depth, (b) Low $\bar{\sigma}$ region extending from 15 to 45 km depth.

In order to better understand SSE in subduction zones such as Cascadia we developed models of dipping faults in an elastic half-space with depth variable friction and effective stress. Elastic Green's functions are computed using a boundary element approach, and the model is driven by deep slip at rate v^{∞}. The depth distribution of frictional properties depends on temperature T [Liu and Rice, 2009]. The friction parameter a ('direct effect') is given by $a = \alpha(T + 273.15)$, where the nominal $\alpha = 3 \times 10^{-5}$, and T is taken from the Peacock [2009] geotherm. Lab friction experiments on gabbros [He et al., 2007] show large scatter, but can be interpreted to show a transition from velocity weakening to strengthening behavior at $T \sim 510$°C. We parameterize $a - b$, as piecewise linear (Fig. 2), with three sections: the surface region is velocity strengthening; at intermediate depth $a - b = 3.5 \times 10^{-3}$; at greater depth friction transitions to velocity strengthening at a depth of ~ 45 km.

Based on seismic imaging studies, which suggest near lithostatic pore-pressures, and uniform property simulations, we take $\bar{\sigma}$ in the depth range 25 to 40 km to be of order 2 MPa. At seismogenic depths, for results shown, $\bar{\sigma} \sim 12$ MPa, while for $z > 40$ km $\bar{\sigma}$ is ~ 120 MPa. The Low Effective-Stress Velocity-Weakening (LESVW) region is where SSE are anticipated to nucleate [Segall et al., 2010, Segall and Bradley, 2012a], and indeed this is observed in simulations. Within the LESVW we take $d_c = 100\mu$m, increasing for numerical reasons to 1 mm updip. The transition in d_c takes place at least 2 km updip of the transition in $\bar{\sigma}$ to prevent artifacts at the effective stress transition.

We found that thermal pressurization overwhelms velocity strengthening friction at depth, causing dynamic ruptures to propagate well into the strengthening region. For this reason, we

suppress thermal pressurization at depth where $a > b$. An increase in shear zone thickness at depth would reduce frictional heating, however we simplify this by artificially increasing the heat capacity. For sufficiently high $\bar{\sigma}$ this is effective at stopping dynamic ruptures. Even without thermal pressurization at these depths, the large thermally induced stress drop in the seismogenic zone drives dynamic rupture into regions with $a > b$ and low $\bar{\sigma}$.

Numerical results fall into two classes, depending on the size of the LESVW relative to the critical nucleation dimension $L_c = d_c\mu'/(\sigma - p^\infty)(b - a)$; for plane strain $\mu' = \mu/(1 - \nu)$. An example where the LESVW is relatively small is shown in Figure 2a. For many decades following a dynamic event the fault is quiescent, with creep penetrating up-dip into the locked zone, at which point SSE spontaneously nucleate. Note that the "transition zone" between the deep fault that creeps at or near the relative plate velocity, and the essentially locked fault, is not static; but rather propagates up-dip as a function of time. The behavior with larger LESVW (relative to L_c) is shown in Figure 2b. Again there is a quiescent period following a dynamic event in which the transition between creeping and locked fault extends up-dip, followed by the spontaneous onset of SSE. The SSE generally propagate up-dip with time; in this case a dynamic slip event nucleates before the SSE reach the up-dip limit of LESVW. Three dynamic events are shown in Figure 2b, only the first and third reach the free surface. The intermediate event is triggered before sufficient stress has accumulated for the rupture to reach the surface.

How do ETS affect the potential for great megathrust events? It is recognized that ETS events increase shear stress on the locked megathrust. Some discussion has been given to whether or not this leads to time varying probability of triggered quakes [Beeler, 2012]. Another possibility, observed in our simulations, is that SSE grow into dynamic ruptures [Segall and Bradley, 2012b]. Understanding which of these occur and how to distinguish between them has implications for assessing time dependent seismic hazard.

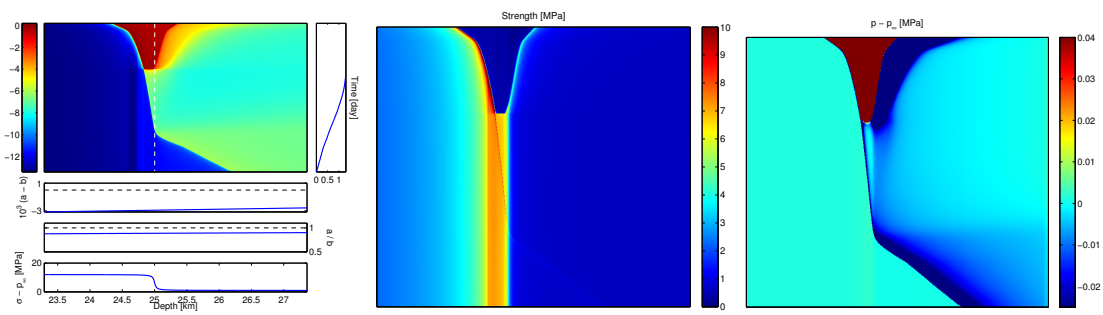

(a) (b) (c)

Figure 3: Zoom in on model in Figure 2a, showing the transition from slow to fast slip. (a) slip speed, $\log_{10}(v)$, (b) fault strength, (c) induced pore-pressure change. Horizontal axis is depth as shown in (a); vertical axis is solver time.

The relationship between slow-slip events and dynamic ruptures is quite different in the two examples shown in Figure 2. The behavior for the small LESVW region is illustrated in more detail in Figure 3. As successive SSE terminate at the up-dip end of the low $\bar{\sigma}$ region they generate a stress concentration at the edge of the locked zone. Toward the end of the interseismic cycle SSE propagate slightly into the higher $\bar{\sigma}$ region. While the details vary, slow slip at higher $\bar{\sigma}$ generates significantly more heat than slip in the low $\bar{\sigma}$ region. As the ultimate SSE penetrates the higher $\bar{\sigma}$ region thermal pressurization induces an increasing loss of strength and the rupture becomes unstable. The ensuing stress concentration at the rupture tip allows

the dynamic slip event to propagate into the locked zone with only modest (few MPa) stress drop.

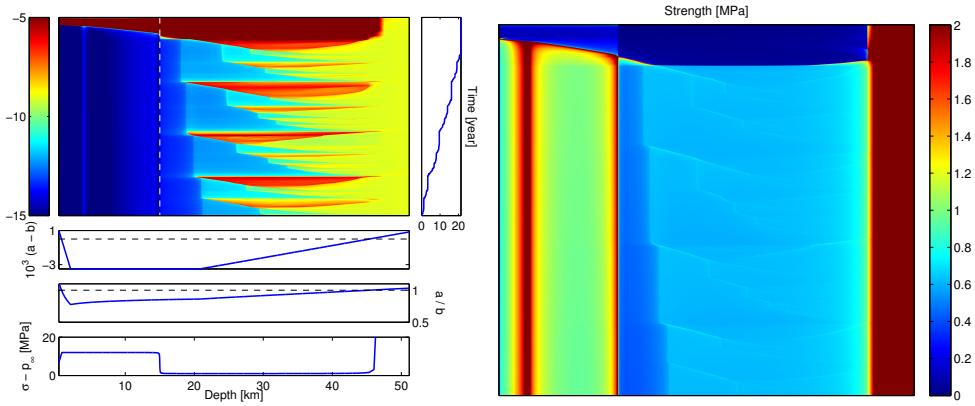

(a) (b)

Figure 4: Zoom on Fig. 2b, showing (a) slip speed, $\log_{10}(v)$, and (b) shear stress for the last several SSE prior to a dynamic event. Horizontal axis is depth as shown in (a); vertical axis is solver time. Stress concentration at the tip of previous dynamic event (Fig. 2b) occurs at ~ 5 km depth.

Nucleation of a dynamic event in the large LESVW case is shown in Figure 4. As in Figure 2b the SSE generally increase slightly in length with time. The maximum slip-speed during an SSE is an increasing function of rupture length [Segall et al., 2010], such that the maximum slip speeds increase slightly with time. In addition, because frictional properties are temperature dependent, $a - b$ becomes increasingly negative up-dip. Thus, the SSE enter a region that is frictionally less stable as they lengthen. The onset of the ultimate SSE is unremarkable, however the slip-speed eventually reaches a point where thermal pressurization becomes a significant weakening mechanism. At this point slip accelerates to inertially limited speeds *within* the SSE zone and then propagates up-dip into the higher $\bar{\sigma}$ region. It is worth noting that although there are stress concentrations both at the edge of the LESVW region and due to the previous dynamic event, the fast slip nucleates deeper within the LESVW region.

What is the downdip limit of megathrust events and how does this relate to the depth distribution of ETS events? Some inversions of geodetic data have placed the downdip limit of locking near the coastline, at depths of $\sim$ 20km [Flück et al., 1997]. This leaves a gap between the bottom of the locked zone and the top of the ETS zone. Others have found that partial coupling extends nearer to the top of the ETS zone [Chapman and Melbourne, 2009, McCaffrey, 2009]; however, both studies require inter-ETS slip *above* the ETS zone.

We explored how predictions of the physical models compare to GPS results. Attention is restricted to the Olympic Peninsula - southern Vancouver Island region, since it is least effected by forearc rotation. We use 29 stations with data from 2002 to 2010, and fit each time series to a constant inter-ETS velocity with variable offset during ETS events. Dates of ETS were taken from the literature and cataloged major tremor episodes. Sample time series fits are shown in Fig. 5b. Finally, we compare the mean-ETS displacement field to predictions of the average model ETS slip distribution. The comparisons are based on a pseudo-3D approach that employs 3D elastic Green's functions. The plate interface model is tessellated using triangular dislocations. Slip at each point on the fault is taken from the 2D physical model at the corresponding depth, which effectively drapes the 2D slip distribution onto the fault.

Since the physics-based model is plane-strain (2D), we must account for the limited along-strike extent of ETS. We taper slip along strike as $[1 - (x/l)^2]^{3/2}$, $l = 150$ km. This yields

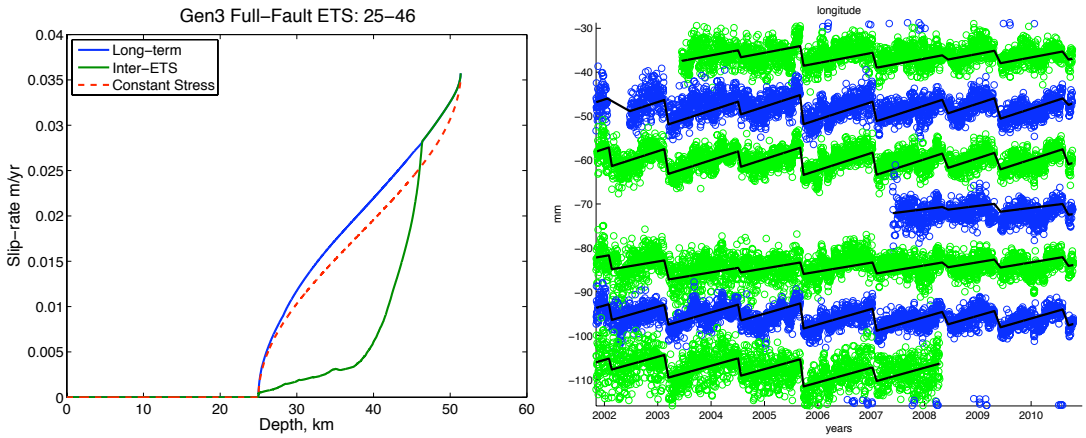

Figure 5: a) Model slip-rate distribution vs depth. "Inter-ETS", shows results between SSE; "Long-term" denotes averaged over may model SSE events, including SSE slip; "Constant Stress" shows analytical result for fault locked for $z < 25$ km, slipping at the plate velocity for $z > 51$ km, and slipping at constant shear stress in the intervening depths. b) Sample GPS time series and fits assuming constant inter-ETS rate but variable offset during ETS events. GPS positions courtesy of T. Melbourne, PANGA.

a satisfactory fit to the displacements, without influencing the depth dependence of slip. Slip is also restricted to be in the plate convergence direction. The fit to the observations using the inferred distributions of frictional properties and effective normal stress is remarkably good (Figure 6). The vertical displacements (not shown) are quite noisy, however the model fits the sign of the vertical displacements at over 80% of the stations. This suggests that the low effective stress – velocity weakening region is in roughly the correct depth range. The mean inter-ETS repeat time for this model is 19 months.

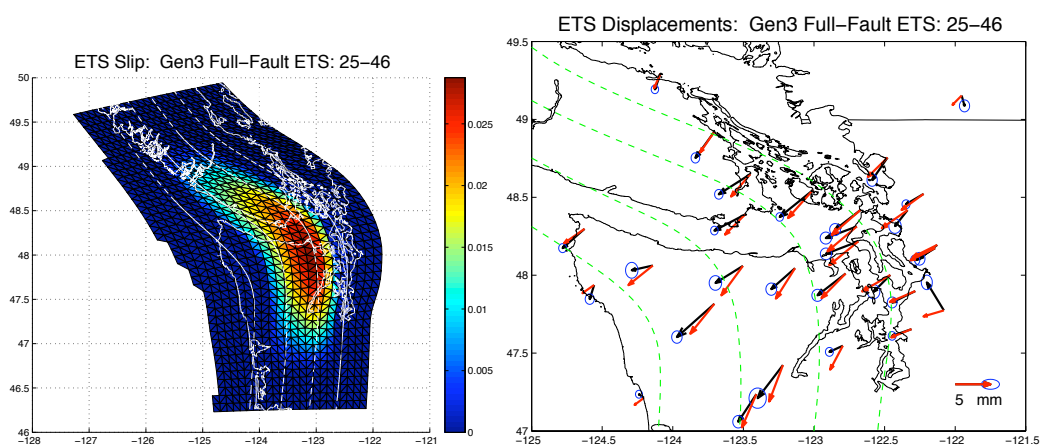

Figure 6: a) Mean model SSE slip, arbitrarily tapered along strike. b) Mean observed ETS displacements, black with 95% confidence ellipses (from sample variance about mean), compared to mean model ETS displacement (red). Contour lines on plate interface at 20, 30, 40, and 50 km depth.

We next compare the predicted inter-ETS slip-rate, which is nearly locked to $\sim$ 40 km (Fig 5), to inter-ETS GPS velocities. We find that model predictions fit the data in the eastern part of the network well, but over-predict the motions on the Olympic Peninsula. This implies that the physics based model has too much locking. Since, formal inversion with physics-based

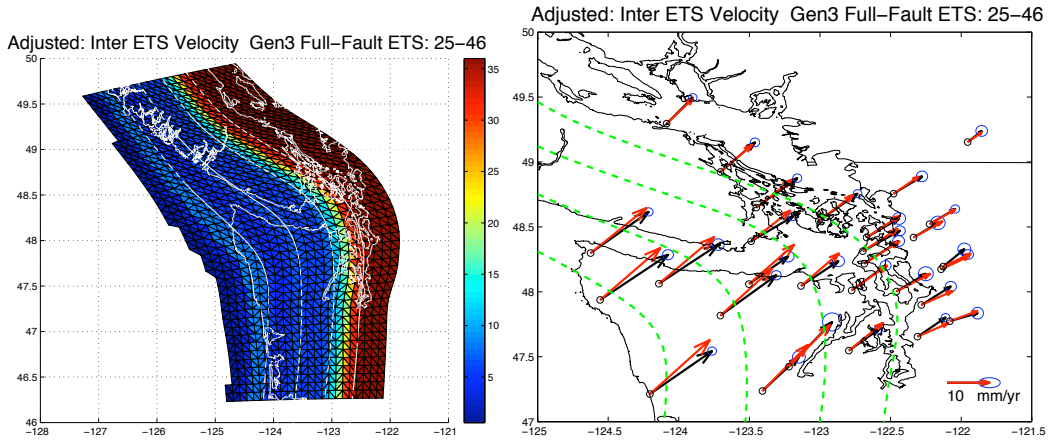

Figure 7: a) Predicted inter-ETS slip-rate distribution after minimum norm correction chosen to fit the data to within 1 mm/yr. b) Observed (black) and predicted (red) velocities. Contour lines as in Fig. 6.

models is not yet feasible, given the intensive forward calculations, we seek a different approach. To get an idea of how the depth-variable properties need to be modified to better fit the data, we conducted kinematic inversions of the *residuals* of the physics-based prediction, for minimum-norm corrections to the inter-ETS slip-rate. That is, we seek the smallest possible kinematic correction to the physics-based model. Since properties are assumed to vary with depth only, we take basis functions corresponding to uniform slip over fixed depth intervals. The preferred estimate is one with least model norm that fits the the data to within ~ 1 mm/yr rms. We find that only modest corrections of ≤ 12 mm/yr, are needed to achieve an acceptable data fit (Fig. 7). Surprisingly, the extra slip is relatively shallow, at $\lesssim 20$ km depth. This interpretation is not unique; it does indicate, however, that we can not reject the hypothesis that the fault is nearly locked between ETS events to a depth of ~ 40 km based on these data.

At present we have no explanation for why creep would occur at this depth. There is no obvious motivation for velocity strengthening behavior in this depth range. Further work is needed to explore both alternative kinematic interpretations, and physics-based explanations for the apparent creep. It is possible that, under appropriate conditions, stable sliding can occur up-dip of the ETS zone even with velocity weakening friction. However, this can only occur over a significant depth range if the local h^* is large, implying either nearly velocity neutral friction, large d_c, or low effective stress. Further work is required to carefully examine the range of conditions where creep updip of SSE occurs and whether this is consistent with geodetic observations.

Improved numerical methods, including extension to 3D. We had proposed (and completed) including the effects of flash heating, and finite thickness shear zones, as well as extending the numerical methods to 3D (2D fault). Although we have not yet begun to thoroughly explore 3D models, this capability now allows far more realistic modeling of SSE nucleation and along strike propagation. Our 3D modelling software is implemented in two packages: `hmmvp` and `fdra2c`.

`hmmvp` forms and applies a hierarchical-matrix (H-matrix [Bebendorf, 2008]) approximation to a boundary element method (BEM) matrix. In our case the BEM matrix represents the linear relationship between displacement on a discretized fault element and stress at every other element center. If a fault is discretized into n elements, n^2 numbers must be stored to represent the BEM matrix exactly. `hmmvp` approximates the matrix by $O(n \log n)$ numbers. A

matrix-vector product (MVP) takes $O(n \log n)$ operations.

In practice we work with faults discretized into tens of thousands to ten million elements. In one example application, the BEM operator for a fault discretized into 6.6 million elements would require 40.0 TB of memory in single precision, while the approximate operator requires 6.8 GB. For more details, see our 2012 AGU poster (`http://www.stanford.edu/~ambrad/pagu12.pdf`)

`hmmvp` has main parts: compression and the matrix-vector product. This year, we parallelized the matrix-vector product using MPI; previously, we had an OpenMP implementation only. Second, we implemented a much faster compressor, again using C++ and MPI. On a shared-memory system having 16 2.6 GHz AMD Opteron processors and 32 GB of memory, it is 19.3 times faster than the previous MATLAB-based compressor on a problem having 40 thousand elements. On larger problems, the speedup is as much as 25x to 30x. This speedup means we can compress exploration-sized problems in minutes rather than hours, and highly resolved problems (one to ten million elements) in one to four hours, rather than two days. The speedup comes from two sources: MPI parallelization (up to a factor of 16 on our system), and C++ rather than MATLAB code (1.5 to 2).

`fdra` is our 2D modelling package. It simulates a rate-state-friction, quasidynamic 1D fault embedded in a 2D halfspace. It also implements diffusion processes for thermal pressurization and dilatancy. It is implemented in MATLAB; most of the computation time is spent in `mex` routines parallelized using OpenMP. Last year we implemented `fdra2`, which uses `hmmvp` to perform the stress-displacement calculation, again in MATLAB and using `mex` routines. It was meant as an intermediate step to an efficient 3D package. This year, we implemented `fdra2c` in C++ and parallelized it using MPI. `fdra2c` has two practical advantages over `fdra2`. First, because it is implemented purely in C++ rather than a mix of MATLAB and C++, the memory use is precise and as small as possible. Second, it is faster, and it scales to more processors. For example, on our 16-CPU system, and for the problem having 6.6 million elements, `fdra2c` is 4.3 times faster than `fdra2c`. We have not implemented the diffusion processes yet. An animated gif of the log of slip speed in a simulation is shown here: `http://www.stanford.edu/~ambrad/ex.gif`.

We show a preliminary simulation, run while developing the software `fdra2`, the 3D version of `fdra`, where only the ETS zone is simulated. In 2D it was observed that model SSE often proceed in two phases: first a slow phase, then a fast [Segall et al., 2010, Segall and Bradley, 2012a]. The same occurs in our 3D simulations. Fig. 8 shows slip speed, friction coefficient, deviation from steady state, and pore-pressure perturbation at five epochs: before the slow phase, during the slow phase, between phases, during the fast phase, and after. During the slow phase stress accumulates on the shallowest part of the fault $x < 180$, while most of the fault is brought to near steady state. During the fast slip phase, dilatant suctions near the rupture fronts, stabilize slip, and stress drops over the shallow fault, leaving it well below steady-state. Hence 3D results, though more complex in behavior, share significant qualitative properties with 2D simulations.

2 Bibliography supported by this grant, exclusive of abstracts

1. A. M. Bradley. H-Matrix and block error tolerances. Technical Report arXiv:1110.2807v1 [math.NA], 2011.

2. Noel M. Bartlow, Shin'ichi Miyazaki, Andrew M. Bradley, and Paul Segall. Space-time correlation of slip and tremor during the 2009 cascadia slow slip event. *Geophys. Res. Lett.*, 38(18):L18309–, September 2011. ISSN 0094-8276.

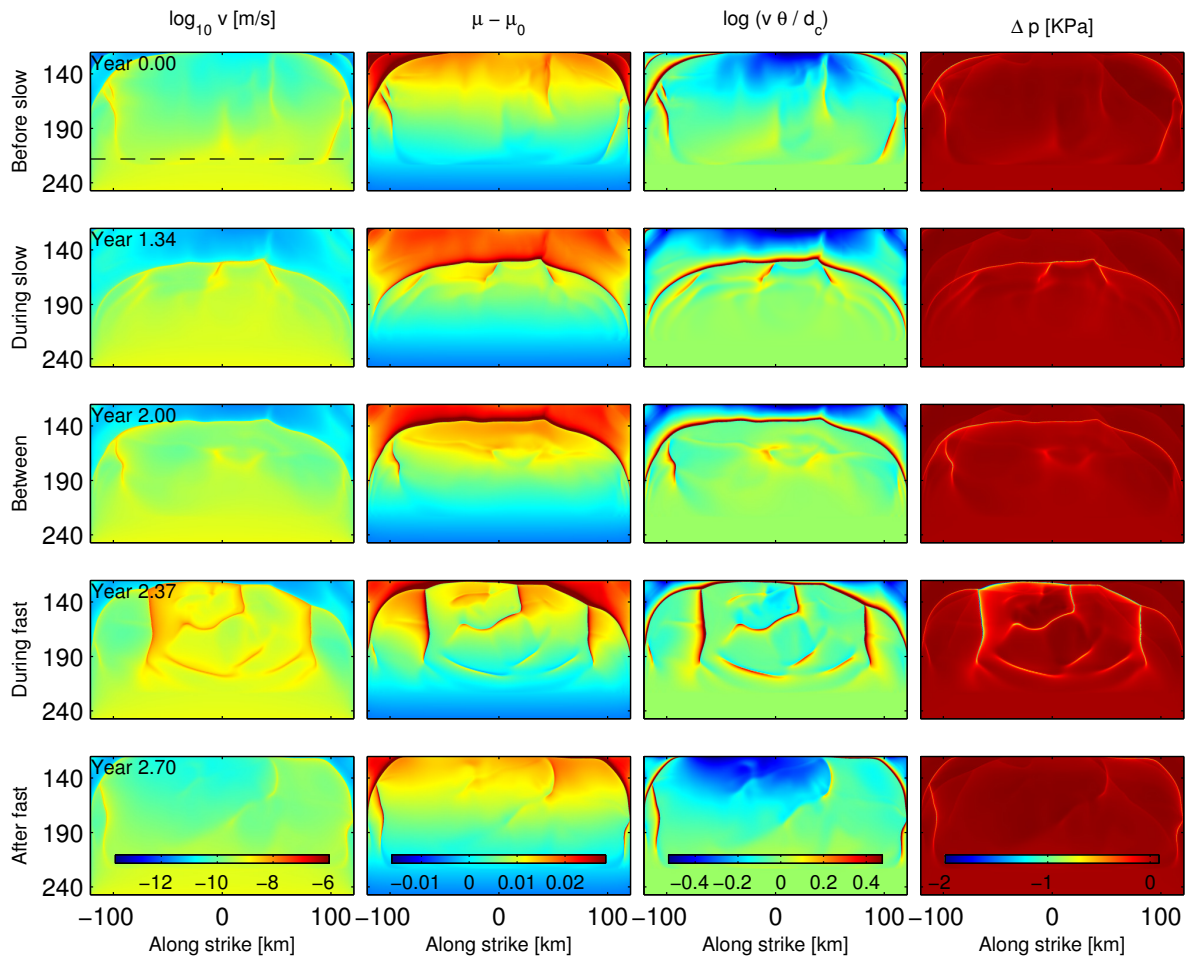

Figure 8: Slip speed, friction coefficient, deviation from steady state $\log(v\theta/d_c)$, and pore-pressure perturbation at five phases of an SSE, as indicated by the title on the left of each row. Time increments between images are indicated. The strike direction (horizontal) extends 241.8 km, and the dip direction extends from $x = 120.2$ (25.00 km deep) to 241.7 km (51.38 km). In the top-left plot, the dashed line indicates the transition between v-weakening and strengthening friction (depth = 45.46 km).

3. P. Segall and A. M. Bradley. Slow vs fast slip due to competition between thermal pressurization and dilatant strengthening. *J. Appl. Mech.*, 79:doi:10.1115/1.4005896., 2012a.

4. P. Segall and A. M. Bradley. Slow-slip triggering of dynamic rupture in 2d numerical simulations. *Geophysical Research Letters*, 39(18):L18308, 2012b.

References

M. Bebendorf. *Hierarchical Matrices: A Means to Efficiently Solve Elliptic Boundary Value Problems*. Springer, 2008.

N. Beeler. Re-estimated effects of deep episodic slip on the occurrence and probability of great earthquakes in Cascadia: delayed failure. *Bull. Seis. Soc. Am.*, in review, 2012.

A. M. Bradley. H-Matrix and block error tolerances. Technical Report arXiv:1110.2807v1 [math.NA], 2011.

A. M. Bradley. H-matrix compression of elastic green's function arrays: Algorithms and error analysis. *Bull. Seis. Soc. Am.*, in prep, 2012.

J.S. Chapman and T.I. Melbourne. Future Cascadia megathrust rupture delineated by episodic tremor and slip. *Geophysical Research Letters*, 36(22):L22301, 2009.

P. Flück, R. D. Hyndman, and K. Wang. Three-dimensional dislocation model for great earthquakes of the Cascadia subduction zone. *J. Geophys. Res.*, 102:20539–20550, 1997.

C. He, Z. Wang, and W. Yao. Frictional sliding of gabbro gouge under hydrothermal conditions. *Tectonophys.*, 445:353– 362, 2007.

Y-J Liu and J. R. Rice. Slow slip predictions based on granite and gabbro friction data compared to GPS measurements in northern Cascadia. *J. Geophys. Res.*, 114, 2009. doi: 10.1029/2008JB006142.

C. Marone and B. Kilgore. Scaling of the critical slip distance for seismic faulting with shear strain in fault zones. *Nature*, 362:618–621, 1993.

C. Marone, C.B. Raleigh, and C.H. Scholz. Frictional behavior and constitutive modeling of simulated fault gouge. *J. Geophys. Res.*, 95:7007–7025, 1990.

R. McCaffrey. Time-dependent inversion of three-component continuous gps for steady and transient sources in northern Cascadia. *Geophys. Res. Lett*, 36:L07304, 2009.

Y. Okada. Internal deformation due to shear and tensile faults in a half-space. *Bull. Seism. Soc. Am.*, 82, 1992.

S.M. Peacock. Thermal and metamorphic environment of subduction zone episodic tremor and slip. *J. Geophys. Res.*, 114:B00A07, 2009.

J. Samuelson, D. Elsworth, and C. Marone. Shear-induced dilatancy of fluid-saturated faults: Experiment and theory. *J. Geophys. Res.*, 114:B12404, 2009. doi: 10.1029/2008JB006273.

P. Segall and A. M. Bradley. Slow vs fast slip due to competition between thermal pressurization and dilatant strengthening. *J. Appl. Mech.*, 79:doi:10.1115/1.4005896., 2012a.

P. Segall and A. M. Bradley. Slow-slip triggering of dynamic rupture in 2d numerical simulations. *Geophysical Research Letters*, 39(18):L18308, 2012b.

P. Segall, A. Rubin, A. M. Bradley, and J.R. Rice. Dilatant strengthening as a mechanism for slow slip events. *Jour. Geophys. Res.*, 115:37, 2010. doi: 10.1029/2010JB007449.

Paul Segall and James R. Rice. Dilatancy, compaction, and slip instability of a fluid-infiltrated fault. *J. Geophys. Res.*, 100(B11):22155–22171, 1995.